



Comparative evaluation of operational land imager sensor on board landsat 8 and landsat 9 for land use land cover mapping over a heterogeneous landscape

Shahfahad, Swapan Talukdar, Mohd Waseem Naikoo, Atiqur Rahman, Alexandre S. Gagnon, Abu Reza Md Towfiqul Islam & Amirhosein Mosavi

To cite this article: Shahfahad, Swapan Talukdar, Mohd Waseem Naikoo, Atiqur Rahman, Alexandre S. Gagnon, Abu Reza Md Towfiqul Islam & Amirhosein Mosavi (2023) Comparative evaluation of operational land imager sensor on board landsat 8 and landsat 9 for land use land cover mapping over a heterogeneous landscape, Geocarto International, 38:1, 2152496, DOI: [10.1080/10106049.2022.2152496](https://doi.org/10.1080/10106049.2022.2152496)

To link to this article: <https://doi.org/10.1080/10106049.2022.2152496>



© 2023 The Author(s). Published by Informa UK Limited, trading as Taylor & Francis Group



Published online: 16 May 2023.



[Submit your article to this journal](#)



Article views: 1054



[View related articles](#)



[View Crossmark data](#)



Citing articles: 2 [View citing articles](#)



Comparative evaluation of operational land imager sensor on board landsat 8 and landsat 9 for land use land cover mapping over a heterogeneous landscape

Shahfahad^a , Swapan Talukdar^a , Mohd Waseem Naikoo^a , Atiqur Rahman^a , Alexandre S. Gagnon^b , Abu Reza Md Towfiqul Islam^c and Amirhosein Mosavi^d

^aDepartment of Geography, Faculty of Natural Sciences, Jamia Millia Islamia, New Delhi, India;

^bDepartment of Geography, Liverpool John Moores University, Liverpool, United Kingdom;

^cDepartment of Disaster Management, Begum Rokeya University, Rangpur, Bangladesh; ^dObuda University, Budapest, Hungary

ABSTRACT

Since its advent in 1972, the Landsat satellites have witnessed consistent improvements in sensor characteristics, which have significantly improved accuracy. In this study, a comparison of the accuracy of Landsat Operational Land Imager (OLI) and OLI-2 satellites in land use land cover (LULC) mapping has been made. For this, image fusion techniques have been applied to enhance the spatial resolution of both OLI and OLI-2 multispectral images, and then a support vector machine (SVM) classifier has been used for LULC mapping. The results show that LULC classification from OLI-2 has better accuracy than OLI. The validation of classified LULC maps shows that the OLI-2 data is more accurate in distinguishing dense and sparse vegetation as well as darker and lighter objects. The relationship between LULC maps and surface biophysical parameters using Local Moran's I also shows better performance of the OLI-2 sensor in LULC mapping than the OLI sensor.

ARTICLE HISTORY

Received 23 May 2022

Accepted 22 November 2022

KEYWORDS

Landsat; land use land cover; surface biophysical parameters; machine learning; artificial intelligence

1. Introduction

Land use land cover (LULC) mapping is critical for assessing the current status of the landscape and how it changes over time (Stephens et al. 2019; Ellis et al. 2021). The LULC mapping has become essential in measuring various features and processes on the earth's surface, like modelling urban extent and expansion (Rahman et al. 2011; Das et al. 2021), land and water quality monitoring (Ritchie et al. 2003), environmental vulnerability and impact assessments (Shahfahad et al. 2020), natural disaster and hazard assessment (Adnan et al. 2020), etc. As a result, monitoring of LULC changes is highly warranted, especially when population and economy are rapidly growing in the developing countries

CONTACT Atiqur Rahman rahman-arahman2@jmi.ac.in Department of Geography, Faculty of Natural Sciences, Jamia Millia Islamia, New Delhi, India

© 2023 The Author(s). Published by Informa UK Limited, trading as Taylor & Francis Group

This is an Open Access article distributed under the terms of the Creative Commons Attribution License (<http://creativecommons.org/licenses/by/4.0/>), which permits unrestricted use, distribution, and reproduction in any medium, provided the original work is properly cited. The terms on which this article has been published allow the posting of the Accepted Manuscript in a repository by the author(s) or with their consent.

(Winkler et al. 2021; Naikoo et al. 2022). The landscape undergoes transformation, and the quantification and management of these transformations are the central theme of the LULC studies (Lambin and Meyfroidt 2011). However, the LULC classification and its quantification are time and money consuming exercises requiring high precision and accuracy, which are difficult to achieve in terrestrial or field-based mapping (Chen et al. 2017; Talukdar et al. 2020).

With the advent of satellite remote sensing technology in the early 1970s, it became easy to map and monitor the earth's surface in a short time (Congalton 2010; Fu et al. 2020). Since then, a number of satellites have been launched to monitor the various characteristics of the earth's surface, such as Landsat, SPOT, IRS Resourcesat, MODIS, etc. (Bauer 2020; Fu et al. 2020). The Landsat data series is the first medium-resolution and longest-running continuous satellite system that is being widely used in remote sensing studies (Wulder et al. 2016; Dwyer et al. 2018). The Landsat data series started with the launch of Landsat 1 in 1972, and since then the data collection has been continuous with at least one Landsat satellite in orbit (Wulder et al. 2019). The Landsat sensors have undergone perpetual evolution in their resolution over time, from 4 broad bands to numerous well-positioned wavelength ranges (Masek et al. 2020). The Multispectral Scanner (MSS) mounted on Landsat 1, 2, and 3 had spectral bands of visible and infrared wavelengths that collected data at 60 m resolution at 6-bit quantization (Egorov et al. 2019). The bit quantization increased to 8 and the spectral bands to 7 in the case of Thematic Mapper (TM), which was installed on Landsat 5 and collected data at 30 m (Arvidson et al. 2006). The enhanced thematic mapper (ETM+) installed on Landsat 7 had an additional 15 m panchromatic band and a 60 m thermal infrared band (Goward et al. 2001). The Landsat 8 has a thermal infrared sensor (TIRS) and operational land imager (OLI), which have facilitated the retrieval of atmospheric aerosol properties and cirrus cloud detection as well as improved backward radiometry (Roy et al. 2014; Wulder et al. 2019). Landsat 9 was launched in September 2021 with OLI-2 and TIRS 2, which is an improved version of Landsat 8. The improvements in TIRS 2 include overcoming the 1- to 2-week reprocessing lag incurred while measuring accurate geolocation, as seen in Landsat 8, as well as enhancements in absolute radiometric accuracy, especially in the longest wavelengths (Masek et al. 2020). Landsat 9 OLI-2 has a 14-bit quantization compared to the 12-bit of Landsat 8 OLI, which enables improved signal to noise for darker objects like coastal waters (Masek et al. 2020).

Although both Landsat 8 and 9 are medium-resolution multispectral satellites with 30 m spatial resolution, resolution can be further increased by merging the multispectral bands with the panchromatic band (Hemati et al. 2021). The fusion of multispectral images with panchromatic images increases the spatial resolution of the multispectral image (Malleswara Rao et al. 2020). For example, the spatial resolution of the multispectral image of Landsat data is 30 m, which increases to 15 m after its fusion with the panchromatic image (Mallick et al. 2021). Researchers have applied image fusion techniques like intense hue saturation (IHS), Brovey, wavelet HIS, etc. to improve the spatial resolution of multispectral images through panchromatic bands (Mallick et al. 2021; Oldoni et al. 2021; Talukdar et al. 2021a). In this research, the wavelet-principal component analysis (W-PCA) image fusion technique has been applied for the improvement of multispectral images of Landsat 8 OLI and Landsat 9 OLI-2 data using panchromatic images.

In recent decades, the application of machine learning for LULC classification has gained significance (Abdi 2020; Talukdar et al. 2020; Shih et al. 2021). The machine learning techniques used for LULC classification include both supervised techniques like random forest (RF), support vector machine (SVM), decision tree, etc., as well as

unsupervised techniques like K-means clustering, iterative self-organizing data (ISODATA), etc. (Talukdar et al. 2020). Several studies on LULC classifications have been done using machine learning algorithms in recent times (Talukdar et al. 2020; Chachondhia et al. 2021; Singh et al. 2021; Zhou et al. 2021; Shahfahad et al. 2022). Further studies have been done to compare the performance of different satellite sensors in LULC classification such as Sentinel-2 and Landsat 8 (Ghayour et al. 2021), TerraSAR-X, Radarsat-2 and Envisat-ASAR datasets (Hütt et al. 2016), ResourceSat-1, Landsat 5 and Landsat 7 (Chander et al. 2008) etc. for exploring different aspects of LULC and its changes for planning. Recently, NASA launched the Landsat 9 OLI-2/TIRS-2 earth observation satellite, which is an advanced version of the Landsat 8 OLI/TIRS satellite in terms of radiometric resolution (Lulla et al. 2021; Choate et al. 2022). None of the studies compared the performances of Landsat 8 OLI and Landsat 9 OLI-2 in LULC classification. As per the Landsat 9 User Handbook, the OLI-2 sensor can detect dark objects like water bodies, and vegetation more precisely than the OLI sensor due to its higher radiometric resolution (USGS 2021). At the same time, Landsat 8 and 9 together can provide a new dimension of research for long-term planning and management purposes. Hence, a comparison of its performance with that of Landsat 8 OLI in LULC classification may help future researchers find suitable datasets for LULC mapping. Therefore, the aim of this study is to compare the accuracies of Landsat 8 OLI and Landsat 9 OLI-2 data for LULC mapping over heterogeneous surfaces, i.e. Mumbai, the most populated city of India.

2. Material and method

2.1. Experimental study area

For this experimental study, Mumbai city has been selected as the study area, which is a maritime city located in the western part of India along the Arabian Sea coast (Figure 1). The city has a complex and mixed land use pattern with large-scale heterogeneity, from planned residential and industrial areas to informal slum settlements (Pethe et al. 2014; Rihan et al. 2021). The population of Mumbai has grown from about 3 million in 1951 to more than 18 million in 2011, making it the largest city in India in terms of population (Census of India 2011). Due to this rapid and continuous increase in population, the city has experienced a very fast transformation of its LULC pattern in the last few decades. Mumbai is a maritime city, surrounded by the Arabian Sea from the south and west, Thane Creek from the east, and the mainland of India from the north. Mumbai has a tropical moist climate (Köppen–Af), with a temperature variation of between 44 °C (June) and about 10 °C (January). The mean annual precipitation of the city is about 250 cm (1901–2015), most of which falls during June–August (Praveen et al. 2020). The city has a large reserved forest over the central ridge, which extends from the central parts to the northern edge of the city. Furthermore, it also has sparse mangrove vegetation in the western parts along the Malad and Gorai creeks. It has three major lakes in the central parts of the city (over the central ridge part of the city), which are the main sources of water for domestic use in the city.

2.2. Details of the satellite data used

Since its advent in the 1970s, the Landsat satellite of the National Aeronautics and Space Administration has emerged as the most utilized satellite data in earth surface mapping (Roy et al. 2014; Wulder et al. 2019; Masek et al. 2020). In this study, two of the most

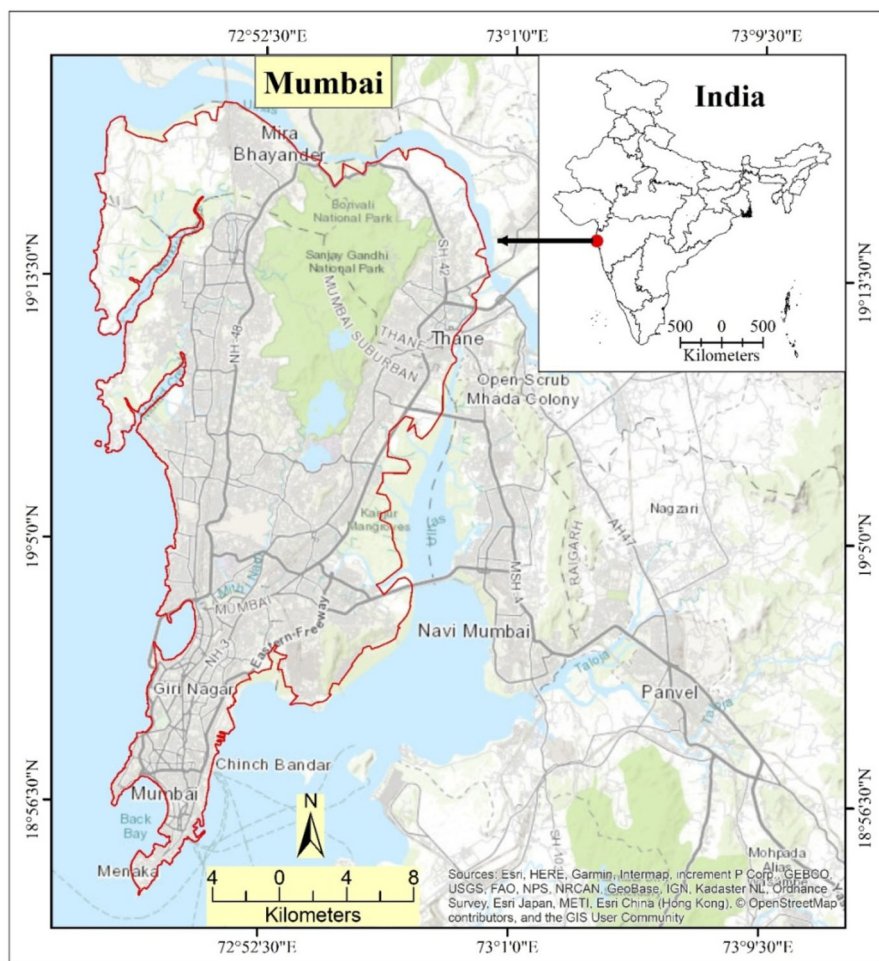


Figure 1. Locational aspect of the experimental study area.

Table 1. Details of the Landsat satellite data used.

Satellite	Sensor	Date of Acquisition	Path/ ROW	Spatial Resolution	Radiometric Resolution	Temporal Resolution	Cloud Cover
Landsat 8	OLI/TIRS	13-02-2022	148/47	30/100	12 bit	16 days	0.03%
Landsat 9	OLI-2/TIRS-2	21-02-2022	148/47	30/100	14 bit	16 days	0.00%

recent satellite data sets of the Landsat program, i.e. Landsat 8 and 9, downloaded from the United States Geological Survey (USGS) website Earth Explorer (<https://earthexplorer.usgs.gov/>), have been utilized for the LULC mapping (Table 1). Over Mumbai, cloud cover is mostly seen due to its tropical-maritime location. Hence, to avoid cloud cover and haze-like conditions, the satellite data of February has been used in this study. Both Landsat 8 and 9 have two sensors, i.e. an operational land imager (OLI) and a thermal infrared sensor (TIRS), and have eleven bands, which comprise eight multispectral bands (with 30 m spatial resolution), two thermal bands (100 m spatial resolution), and a pan-chromatic band (15 m spatial resolution). Landsat 8 is the eighth satellite of the Landsat program (the seventh to reach orbit), which was launched on February 11, 2013. Landsat 9 is the ninth satellite of the Landsat program (the eighth to reach orbit), which was

launched on September 27, 2021. Both Landsat 8 and 9 have a temporal resolution (revisiting time) of sixteen days. Landsat 9 has been placed in orbit in such a way that, together with Landsat 8, it has increased the revisiting period to eight days (Masek et al. 2020). Although both Landsat 8 and 9 have similar band composition and revisiting periods, the main difference is in the radiometric resolution. The OLI sensor of Landsat 8 has 12-bit radiometric resolution, while the OLI-2 sensor of Landsat 9 has 14-bit radiometric resolution, making it more accurate for mapping the spatial differences, especially over the darker objects. With 12-bit data, the Landsat 8 OLI sensor can differentiate 4096 color shades, while with 14-bit data, the Landsat 9 OLI-2 sensor can differentiate 16384 color shades of a given wavelength (USGS 2021). In addition, both sensors provide nine spectral bands with the same wavelength and two TIRS bands (Band 1 Visible (0.43 – 0.45 μm) 30-m, Band 2 visible (0.450 – 0.51 μm) 30-m, Band 3 visible (0.53 – 0.59 μm) 30-m, Band 4 Red (0.64 – 0.67 μm) 30-m, Band 5 Near-Infrared (0.85 – 0.88 μm) 30-m, Band 6 SWIR 1 (1.57 – 1.65 μm) 30-m, Band 7 SWIR 2 (2.11 – 2.29 μm) 30-m, Band 8 Panchromatic (PAN) (0.50 – 0.68 μm) 15-m, Band 9 cirrus (1.36 – 1.38 μm) 30-m). The function of the bands is the same in both OLI and OLI-2 sensors. Overall, the OLI and OLI-2 sensors are almost similar and will provide consistent images of the earth's surface with similar spatial, spectral, geometric, and radiometric qualities. The only difference is the ability of OLI-2 to detect more objects and more precisely because of the higher number of color shades due to better radiometric resolution.

2.3. Method for the satellite data pre-processing and image fusion

Though the Landsat data used in this study were cloud-free, it is still recommended that the satellite data be pre-processed before classification because it may be influenced by atmospheric, topographic, geometric, and sensor errors (Wentz et al. 2014; Young et al. 2017; Phiri et al. 2018). Furthermore, the problems of haze and noise are very common in the tropical maritime regions. Thus, it is highly recommended to perform the pre-processing steps like atmospheric and radiometric corrections, histogram equalization, and the removal of uncertain pixels, such as pixels with cloud cover (Song et al. 2001). The downloaded Landsat datasets, i.e. OLI and OLI-2, were first stacked to get the multispectral images. Further, the haze and noise reduction techniques were performed using the ATCOR extension tool in the ERDAS Imagine software to enhance the quality of the multispectral images as well as to remove atmospheric and radiometric errors from them. Another important pre-processing technique is the image fusion technique, which is used for improving the visual and analytical quality of satellite imagery (Mallick et al. 2021). It is capable of retaining essential information by retrieving all relevant information from photos without causing errors in the resulting image. The fusion of multispectral pictures with panchromatic images is a method of enhancing the resolution of multispectral images by merging the low-resolution MS bands of the same satellite with the high-spatial-resolution Pan band (Mahyari and Yazdi 2011). The most frequently applied image fusion techniques are intensity-hue-saturation (IHS), Brovey transform, wavelet transform, Gram-Schmidt (GS) transform, etc. (Mallick et al. 2021).

Among all the image fusion techniques, W-PCA is a better technique than others (Amolins et al. 2007; Talukdar et al. 2021a) because this technique produces a better result than other techniques like HIS, GS, and PCA. Further, being an integrated model of wavelet and PCA, this model reduces the error of the basic wavelet and PCA techniques (Kaur et al. 2021; Figure 2). Hence, in this study, the W-PCA image fusion

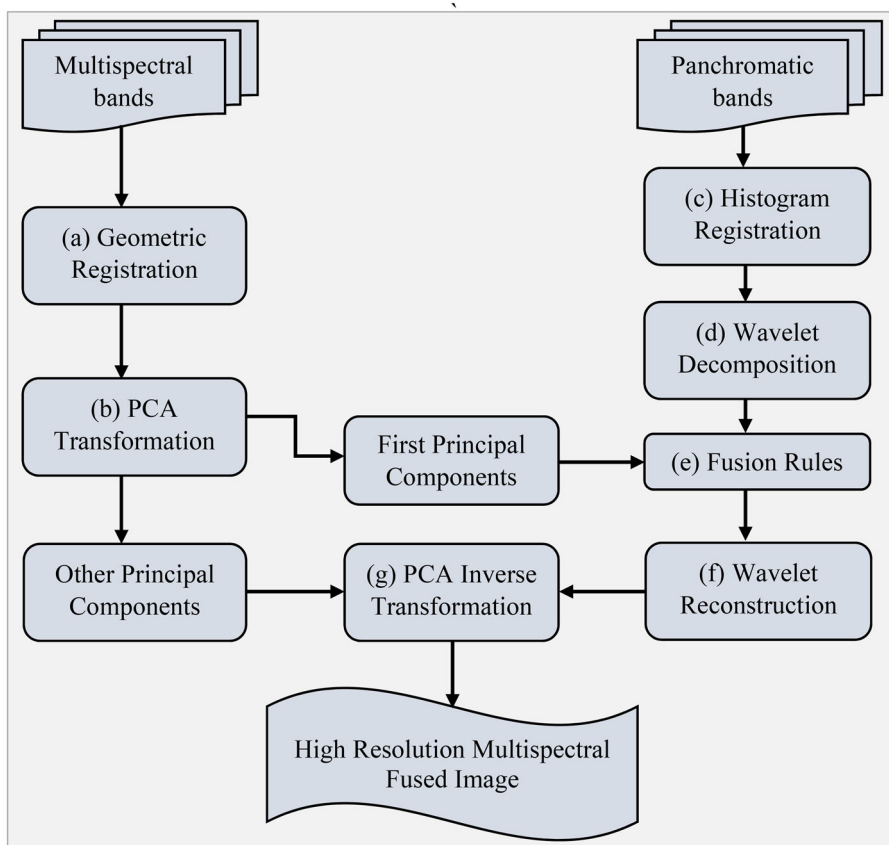


Figure 2. The schematic diagram of the process of wavelet-PCA for generating the high-resolution multispectral images.

technique has been applied to improve the visual and analytical quality of the OLI and OLI-2 multispectral images using ERDAS Imagine software (Figure 3).

A wavelet transform is a mathematical tool that can be applied to fuse images following the concept of multi-resolution analysis (Yunhao et al. 2006). The wavelet-PCA transform method combines the traditional PCA method with the wavelet transform. PCA is initially applied to the MS image, and the first principal component (PC1) is obtained. In the wavelet decomposition, wavelet coefficients are used for each PC1 and new PAN image to generate a half-resolution approximation image with wavelet coefficient images corresponding to horizontal decomposition (HD), vertical decomposition (VD), and diagonal decomposition (DD). Then, the coefficients of the PAN image representing the spatial detail information are injected into the PC1 image through the inverse multi-resolution wavelet decomposition. The new PC1 component is obtained by performing wavelet reconstruction, and then the inverse transform is applied to the image to construct a fused RGB image (Mhangara et al. 2020).

2.4. Method for the LULC classification and accuracy assessment

Several machine learning algorithms have been applied for the LULC classification on satellite data, such as the spectral angle mapper (SAM), the artificial neural network (ANN),

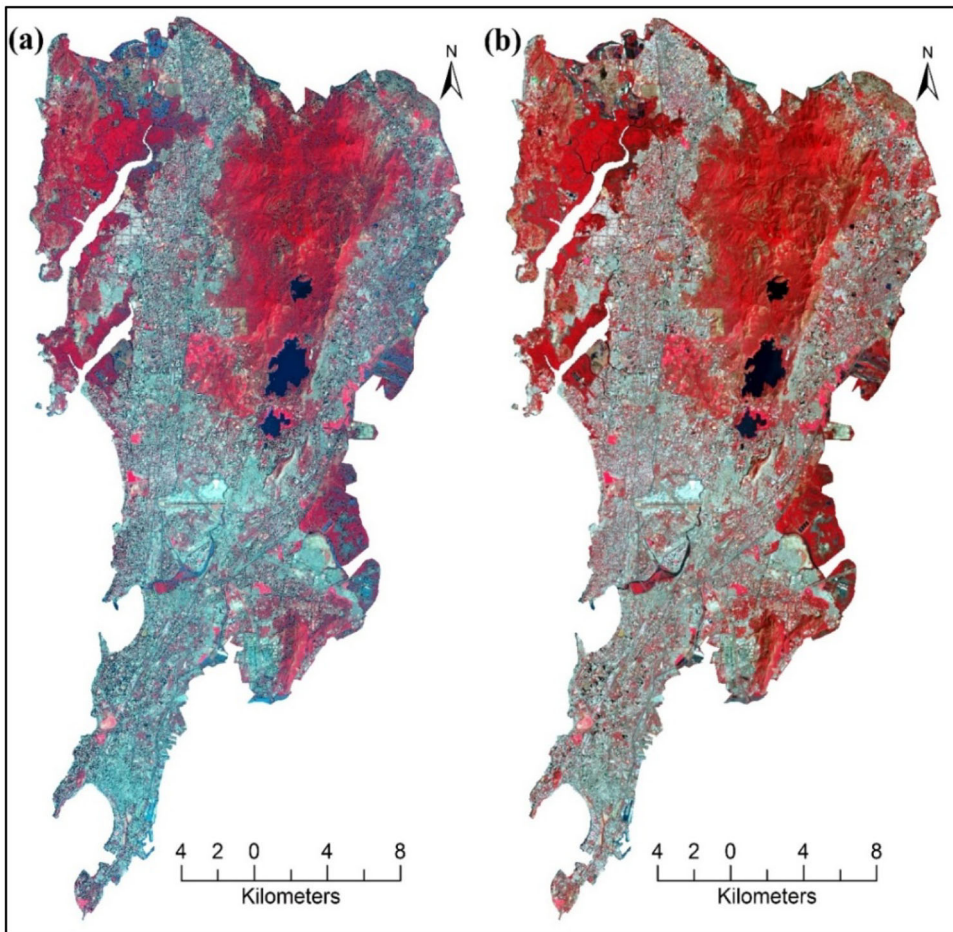


Figure 3. False color composite after fusion of (a) Landsat 8 OLI and (b) Landsat 9 OLI-2 data.

the RF, the SVM, etc. Based on a comprehensive review of the application of machine learning algorithms and comparing six machine learning algorithms i.e. SVM, RF, ANN, Fuzzy ARTMAP, SAM and Mahalanobis distance (MD) in LULC classification, Talukdar et al. (2020) found that SVM and RF are the best algorithms for LULC classification. Therefore, in this study, SVM is used to make LULC classification using the OLI and OLI-2 datasets. The SVM is founded on the idea of structural risk mitigation (SRM), which divides data points into different classifications using a hyper-spectral plane. The vectors in this procedure assure that the size of the margin is maintained (Noble 2006). The SVM may incorporate various continuous and categorical variables along with linear and non-linear samples with varying class labels. Support vectors are the surrounding samples that designate the boundary or hyperplane of SVM (Talukdar et al. 2020; Yılmaz et al. 2022). The SVM model has been utilized to classify the LULC based on the training sample and layer-stacked input variables. To run the mode, the C-support vector has been applied in this study. The SVM is executed with the following parameters of; the penalty parameter (C) of 1, Nu of 0.5, P of 0.5, the radial basis function-based kernel, the coefficient 0 of 1, the degree of 0.5, and the gamma of 1. Based on this optimized parameter, the LULC has been classified for two Landsat images. For the LULC classification, 724 training samples were randomly selected in proportion to the area of each LULC class

in the study area. Separate training samples were collected for both the OLI and OLI-2 datasets using the ArcGIS software. The LULC has been classified into six classes, water bodies, dense vegetation, sparse vegetation, built-up areas, cropland, and open land, based on the NRSC (1995) classification scheme.

The classified LULC maps are subject to accuracy assessment, as for planning and policy framing purposes, high precision LULC maps are required. Thus, the validation of classified LULC maps is considered a significant step in the LULC classification, which describes the precision/correctness of the LULC maps. For the validation of LULC maps, scholars have used different techniques such as root mean square error (RMSE), Kappa coefficient, error matrix, etc. (Adam et al. 2014; Phan et al. 2021; Talukdar et al. 2021b; Naikoo et al. 2022). In this study, the Kappa coefficient was used to assess the accuracy of the LULC classification from the Landsat OLI and OLI-2 datasets.

2.5. Land discrepancy analysis between the LULC maps of OLI and OLI-2

The LULC mapping has been done from the OLI and OLI-2 multispectral images to examine the efficiency of the object detection ability of the sensors. Thus, to examine the object detection ability of the OLI and OLI-2 sensors, a Markovian transition matrix has been applied. This method has often been utilized to compute the land use change analysis among several land use classes for the LULC of two different time periods. Hence, it has been applied to investigate the land discrepancy among different LULC classes between two LULC maps. If the discrepancy among land use classes is greater, it can be stated that both sensors have different object detection abilities at high magnitude. The Markovian transition matrix was used to assign LULC changes from t to $t + 1$. It implies that the range of pixels was expected to convert from any LULC class to any other at some point throughout the specified range of pixel units. The following matrix p was proposed for the depiction of chances (eq. 1).

$$p = pij = \begin{pmatrix} p_{11} & p_{12} & p_{1m} \\ p_{21} & p_{22} & p_{2m} \\ p_{31} & p_{32} & p_{3m} \end{pmatrix} \quad [1]$$

where, p represents the probability of transition from i to j .

2.6. Extraction of surface biophysical parameters

The surface biophysical parameters (normalized difference spectral indices) have been widely used as indicators of the LULC pattern in different parts of the world. Seven surface biophysical parameters were made using the multispectral bands of Landsat 8 and 9 satellites as indicators of LULC pattern as well as to analyze the accuracy of LULC classification. The normalized difference vegetation index (NDVI) is used to assess the distribution and density of vegetation cover in a region (Shahfahad et al. 2020). It is calculated using the near infrared (NIR) and red (R) bands (Kriegler et al. 1969), i.e. band 5 and band 4 of the Landsat 8 and 9 (eq. 2).

$$NDVI = \left\{ \frac{NIR - R}{NIR + R} \right\} \quad [2]$$

Soil adjusted vegetation index (SAVI) is a replacement for NDVI that is calculated using NIR and red (R) bands with a soil adjustment factor L as shown in equation 3 (Huete 1988).

$$SAVI = \frac{(NIR - R)(1 + L)}{(NIR + R + L)} \quad [3]$$

The normalized difference built-up index (NDBI) is used to assess the built-up surfaces and is calculated using NIR and short-wave infrared (SWIR) bands (Zha et al. 2003) as given in equation 4.

$$NDBI = \left\{ \frac{NIR - SWIR}{NIR + SWIR} \right\} \quad [4]$$

With the help of short-wave infrared (SWIR) and thermal infrared (TIR) bands, Chen et al. (2006) used equation 5 to figure out how to calculate the normalized difference bareness index (NDBaI).

$$NDBaI = \left\{ \frac{SWIR - TIR}{SWIR + TIR} \right\} \quad [5]$$

To analyze the surface water bodies and delineate it from other land use types, the normalized difference water index (NDWI) was calculated by using green and NIR bands (McFeeters 1996) as given in equation 6.

$$NDWI = \left\{ \frac{Green - NIR}{Green + NIR} \right\} \quad [6]$$

Further, the modified normalized difference water index (MNDWI) is calculated using the Green and SWIR bands (Xu 2006) as given in equation 7.

$$MNDWI = \left\{ \frac{Green - SWIR}{Green + SWIR} \right\} \quad [7]$$

For the analysis of soil moisture content, the normalized difference moisture index (NDMI) was calculated using NIR and SWIR bands (Jin and Sader 2005) as given in equation 8.

$$NDMI = \left\{ \frac{NIR - SWIR}{NIR + SWIR} \right\} \quad [8]$$

2.7. Relationship between LULC and surface biophysical parameters using bivariate local Moran's I

The bivariate Moran's I have been applied to investigate the relationship between LULC and surface biophysical characteristics in terms of clustering (positive) and dispersion (negative) at a spatial scale. Two kinds of bivariate Moran's I techniques have been widely used for calculating spatial clustering analysis: global bivariate Moran's I and local bivariate Moran's I (bivariate LISA). The bivariate Moran's I provide a measure of the influence of one variable on the occurrence of another variable in its proximity, while the bivariate LISA examines the status of spatial clustering as well as outliers (Anselin et al. 2002). The local bivariate Moran's method was utilized in this work to depict spatial correlations within distinct units per pixel in two LULC maps (Overmars et al. 2003). The LISA was calculated using equation 9.

$$I_{eu} = Z_i^e \sum_{j=1}^N W_{ij} Z_j^u \quad [9]$$

where, I_{eu} is the local bivariate Moran's I for LULC and surface biophysical parameters. W_{ij} is defined as an N -by- N weight matrix at spatial scale between the spatial unit of i^{th} and j^{th} , which have been produced using queen contiguity weight based on the neighbour of first order in a 3×3 matrix. Z_i^e denotes the value of LULC for i^{th} spatial unit, while Z_j^u refers to the value of biophysical parameters at j^{th} spatial unit. However, the value of I_{eu} varies from -1 to 1 . The cluster maps, which show positive and negative spatial relationships, were divided into four kinds of spatial correlation, including two cluster categories: high-high and low-low. If the same high observed values surround a pixel with a high value, the result will be high-high, and if neighbours surround a pixel with a low value with low values, the result will be low-low. Furthermore, the outputs included two outlier categories, which implied negative spatial connection and arose when low values surrounded a high value (high-low) or vice versa (low-high). For example, the positive values denote the positive spatial relationship between LULC and surface biophysical parameters, which implies that a pixel having a high value of LULC in terms of built-up area (if the target is built-up, the value will be 1 and 0 for others; the target variable changes with the changes of surface biophysical parameters) is likely to be surrounded by the high positive value of surface biophysical parameters (NDBI). In contrast, a pixel with a low value, like 0, of LULC for target built-up is likely to be surrounded by the negative value of surface biophysical parameters, like NDBI. Similar conditions will exist for vegetation and other land use features. After modelling the spatial clustering with bivariate local Moran's I, the statistical significance has also been evaluated through permutation tests. We used 999 permutations (default setting for modelling) for the analysis. For the achieved pseudo value, the statistical significance value for spatial correlation has been set to 0.05. The detailed methodology has been presented in the flow chart (Figure 4).

3. Results

3.1. Analysis of the LULC classification using OLI and OLI-2

Based on the National Remote Sensing Centre's (NRSC 1995) level-I classification scheme, six LULC classes were identified in Mumbai i.e. open land, sparse vegetation (scrubs and grasslands), cropland, vegetation cover, built-up area, and water bodies. The analysis of LULC classification shows that, although the built-up area and water bodies had almost similar patterns in the LULC maps classified from both OLI and OLI-2 data, a marked difference has been noted in the pattern of vegetation cover, scrubland, open land, and croplands (Figure 5).

The classified LULC map of Landsat 8 OLI shows a large proportion of area under open land in the central and northern parts of Mumbai. However, in the LULC map of Landsat 9 OLI-2, the area under open land is smaller in the central and northern parts. While comparing the results from Google Earth imagery, it is seen that a large proportion of built-up area has been misclassified as open land in the central parts of the LULC map of Landsat 8 OLI. At the same time, in the LULC map of Landsat 9 OLI-2, a large proportion of open land has been misclassified as built-up area, especially in the northern parts of Mumbai. Similarly, a significant proportion of the densely vegetated areas were misclassified as sparse vegetation in the LULC map of OLI data (Figure 6). On the other hand, the vegetation cover has been classified accurately in the LULC map while using OLI-2 data (Figure 6). This may be due to the higher radiometric resolution of OLI-2 than OLI, which enables it to differentiate and detect darker objects more accurately (Masek et al. 2020; Hemati et al. 2021). It can be seen that at several places, the cropland

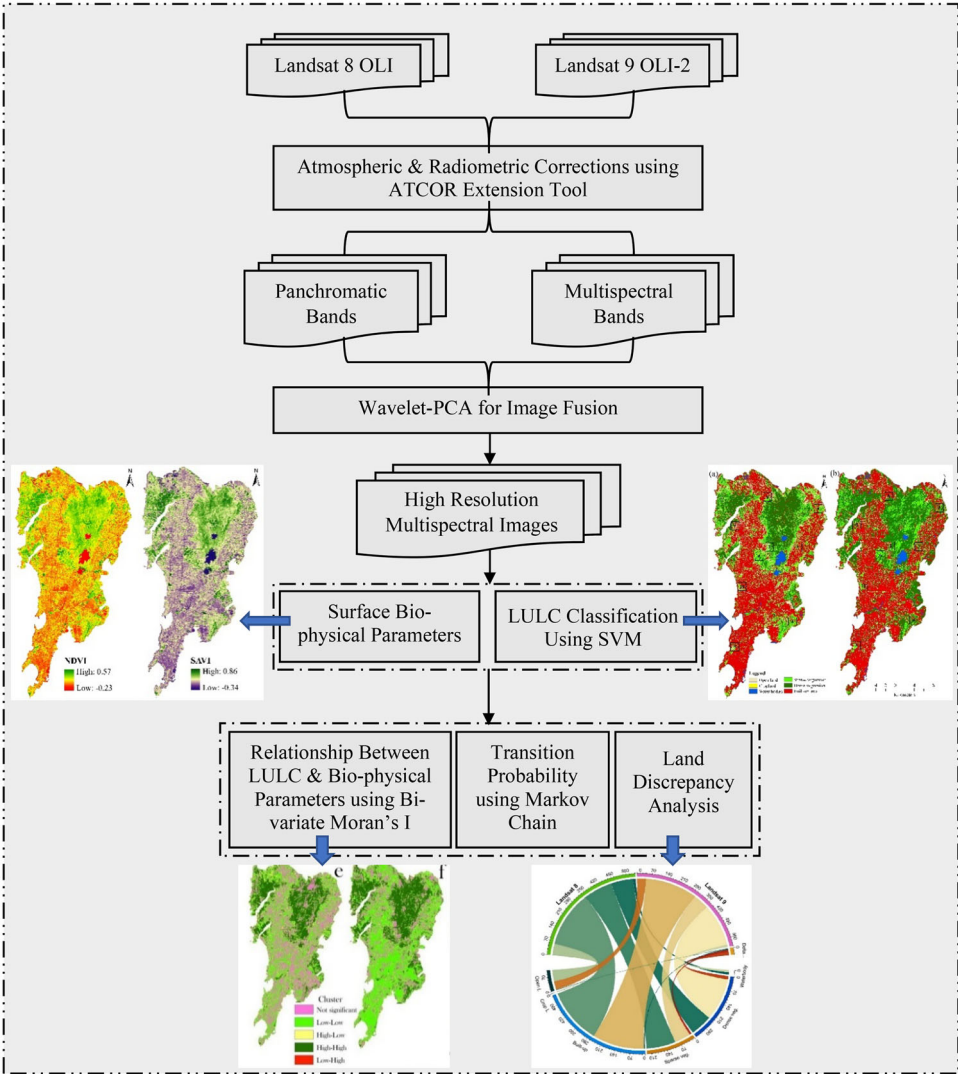


Figure 4. Methodological flow chart for the study.

has been misclassified as scrublands, especially in the central, western, and south-eastern parts of the city.

Mumbai city has a significant proportion of mangrove vegetation, especially along the Malad and Gorai creeks in the western parts and Thane creek in the eastern part (Azeez et al. 2022). The mangrove vegetation in the northern and western parts of Mumbai has been classified as sparse vegetation in the LULC map of OLI data. However, in the LULC maps classified from OLI-2 data, the mangrove vegetation has been clearly differentiated from the sparse vegetation. Similarly, the open land in the form of sand bars in the eastern part of Mumbai city has been classified as the built-up area in the LULC map of OLI data, while it has been clearly classified as open land in the LULC map of OLI-2 data.

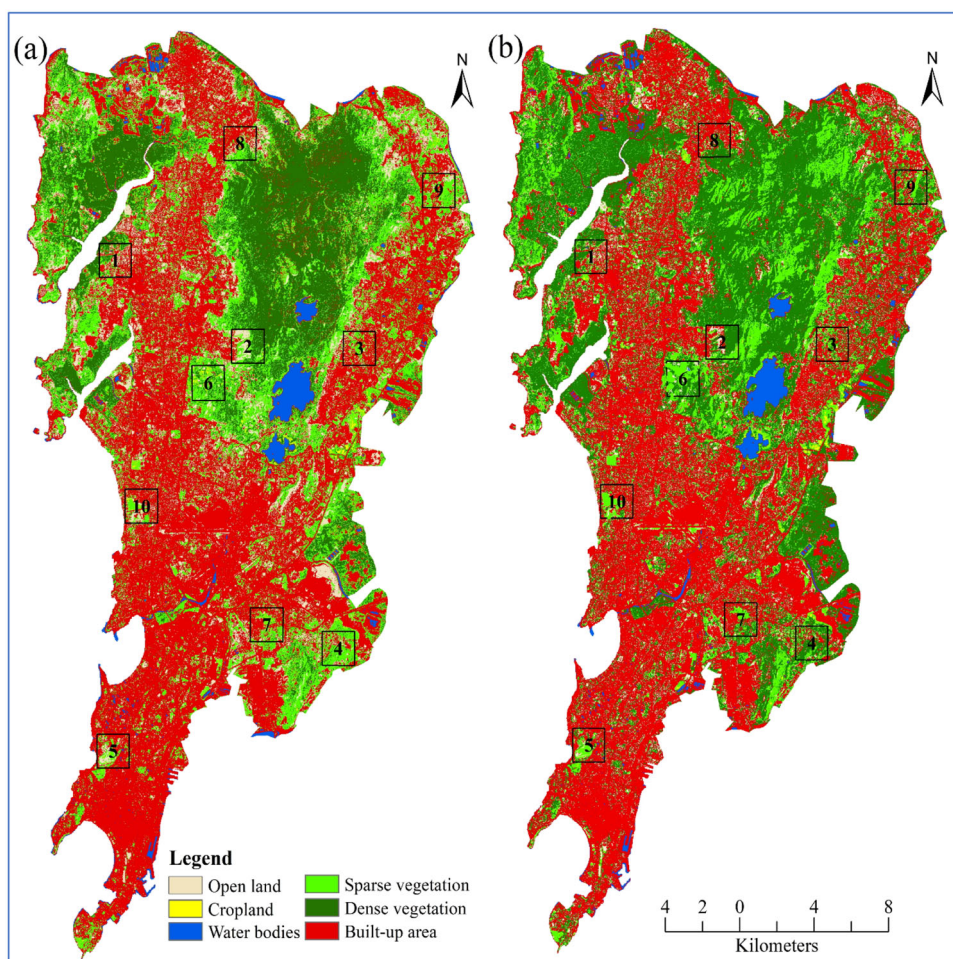


Figure 5. Classified LULC maps using multispectral bands of (a) Landsat 8 OLI and (b) Landsat 9 OLI-2.

3.2. Land detection discrepancy between landsat 8 and landsat 9

In the present study, a land detection discrepancy analysis has been conducted to explore the differences in the ability of the sensors of Landsat 8 OLI and Landsat 9 OLI-2 to detect objects. The Markovian transition matrix along with change detection at the spatial scale have been applied for the land detection discrepancy analysis. [Figure 7](#) shows the land use discrepancy values at varying magnitudes. The diagonal value (both on the x and y axes) between the particular land use classes shows the magnitude of the detection ability of the same land use by the two sensors. For example, the diagonal value of the water body (both in the x and y axes) is 0.8, which indicates that 80% of the water body of the study area has been clearly detected by the sensors, while 20% of the water body has been allocated to the built-up areas ([Figure 7](#)). Similarly, both the sensors have correctly detected all the land use features within 80% of the study area. Therefore, 20% of all features have discrepancies. It indicates that both sensors have some difference in their object detection abilities. To quantify the difference in LULC classification, the detection technique was applied ([Figure 8](#)).



Figure 6. Comparison of the LULC classification with google earth.

Figure 8 shows the change detection analysis at a pixel-by-pixel scale between the LULC maps of the OLI and OLI-2 sensors. Some discrepancies have been observed in dense vegetation, cropland, and sparse vegetation. For example, the OLI image has detected the body of water by 11.86sq. km., while OLI-2 has detected 11.33sq. km. Nevertheless, the change analysis shows that 9.74sq. km of water body areas are common

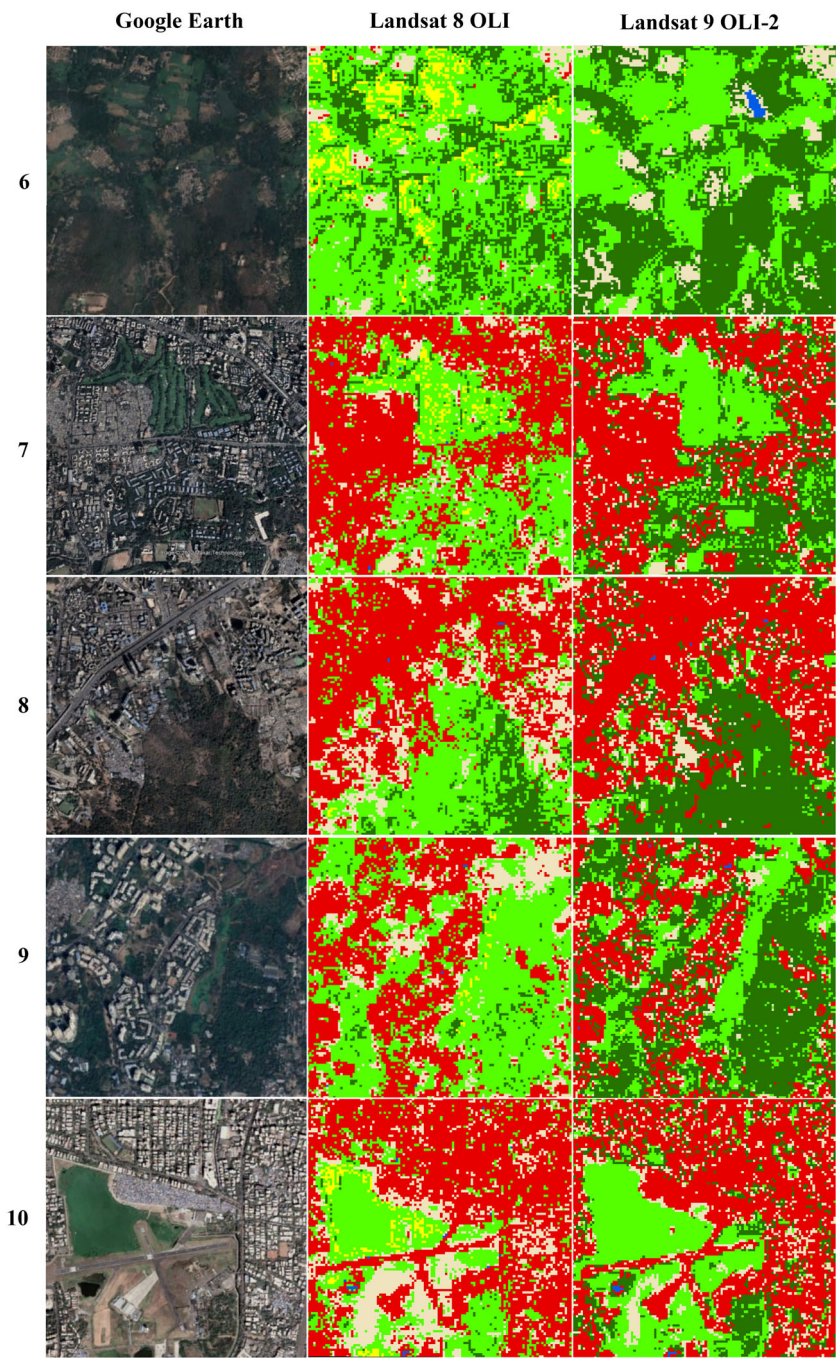


Figure 6. Continued

for both sensors (Figure 9). In the case of OLI, it has detected 1.85 sq. km of the built-up area as a water body, followed by a 0.14sq. km area of dense vegetation. On the other hand, the OLI-2 sensor has detected 1.35 sq. km of the built-up area as a water body, followed by 0.22sq. km of sparse vegetation. Therefore, it can be stated that the OLI-2

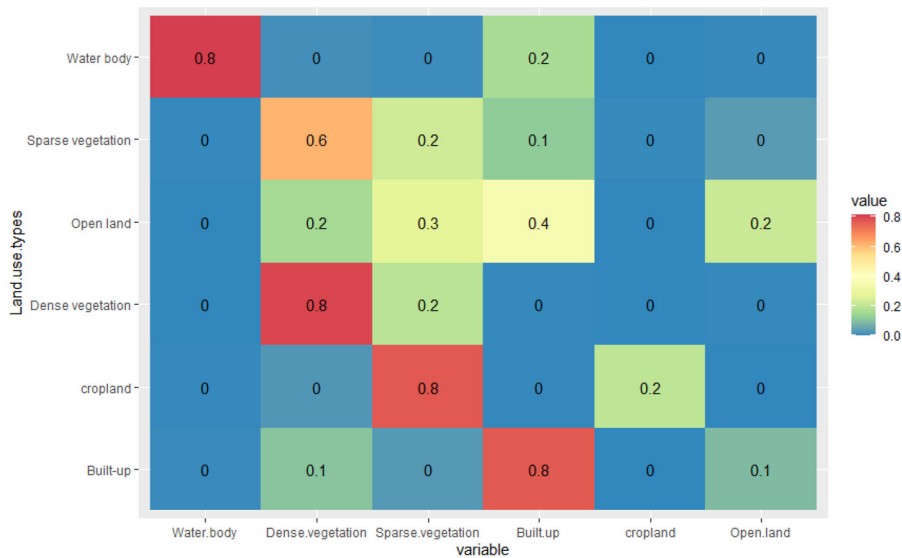


Figure 7. Land discrepancy analysis between Landsat 8 and 9 using Markovian transition matrix.

sensor can detect dark pixels better than Landsat 8. However, in the case of built-up areas, the OLI and OLI-2 sensors have detected 281.49 sq. km and 258.34 sq. km, respectively. In comparison, the average size of the built-up area for both sensors is 220.98 sq. km. This means that both sensors have picked up a large portion of the area differently. For instance, about 19.37 sq. km of open land and 15.91 sq. km of sparse vegetation have been classified as built-up areas in OLI-2. Similarly, in OLI-2, 27.77 sq. km of sparse vegetation have been classified as the built-up area. Hence, it can be stated that OLI-2 detected a significant amount of open land as built-up area. This is because, in many open lands, some kind of construction may be going on; therefore, the spectral values are pretty similar. Moreover, Mumbai has a significant proportion of open land in the form of bare rocky surfaces, especially in the northern parts (Rihan et al. 2021), which generally exhibits spectral values that are pretty similar to the built-up land (Kotthaus et al. 2014; Kamaraj et al. 2021). Furthermore, the sparse vegetation along the open land and the fringe of the built-up area has been detected as built-up area because of the similar spectral values. In contrast, OLI detected most of the discrepant land as having sparse vegetation. Therefore, OLI-2 has more object detection ability than OLI, which can help propose robust management plans for water resources, especially urban management.

3.3. Analysis of the surface biophysical parameters

Figure 10 shows the surface biophysical parameters of Mumbai city calculated using Landsat 8 OLI and Landsat 9 OLI-2 images. The analysis of figure shows that all the indices have an almost identical pattern in both OLI and OLI-2 except NDWI and MNDWI, which show a significant difference, especially in the south-eastern and east central parts. On the other hand, both NDVI and SAVI showed a similar pattern of vegetation cover in Mumbai. In both NDVI and SAVI, the vegetation cover has been detected very high over the central ridge of Mumbai city, which extends from the central part to the northern extreme of the city. At the same time, it varies from low to moderate in the southern parts of Mumbai and very low in the central parts, particularly over the Vihar, Tulsi, and

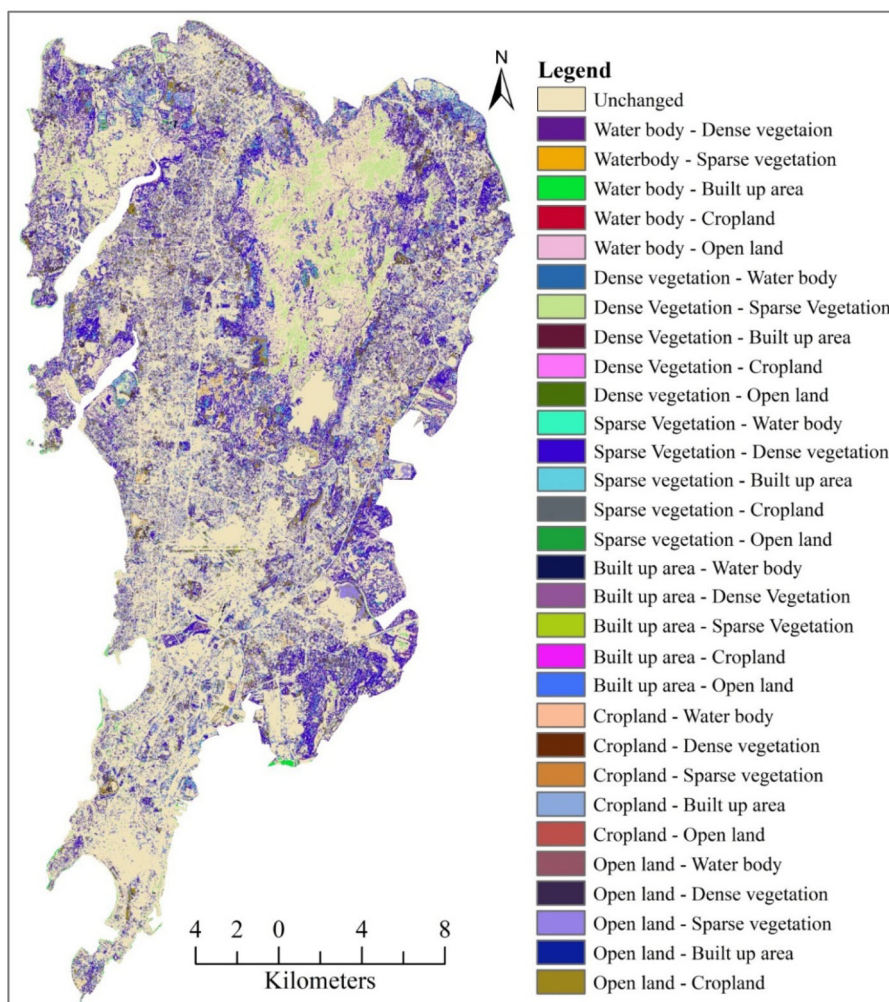


Figure 8. Visualization of spatial discrepancy of land detection between Landsat 8 and Landsat 9.

Powai Lakes. The NDBI shows that the built-up area is high throughout the city except in the northwestern and eastern parts, where it is very low. Further, it is also low over the central ridge, as this part of Mumbai is covered with dense forest. Similarly, NDBaI also shows high bareness throughout the city except in the north-western and eastern parts. Furthermore, the analysis of NDWI and MNDWI shows that the city has very few water bodies in its central, eastern, and northern parts (Figure 10). Moreover, the NDMI shows that the soil moisture is low throughout Mumbai, except in the central, eastern, and north-western parts.

3.4. Validation of the LULC maps

To analyze the reliability and accuracy of the LULC classification from OLI and OLI-2 multispectral images, the accuracy assessment has been done using the kappa coefficient (Tables 2 and 3). The overall accuracy of LULC classification from OLI and OLI-2 was 87.00% and 94.1%, respectively. According to Anderson (1976), for successful and

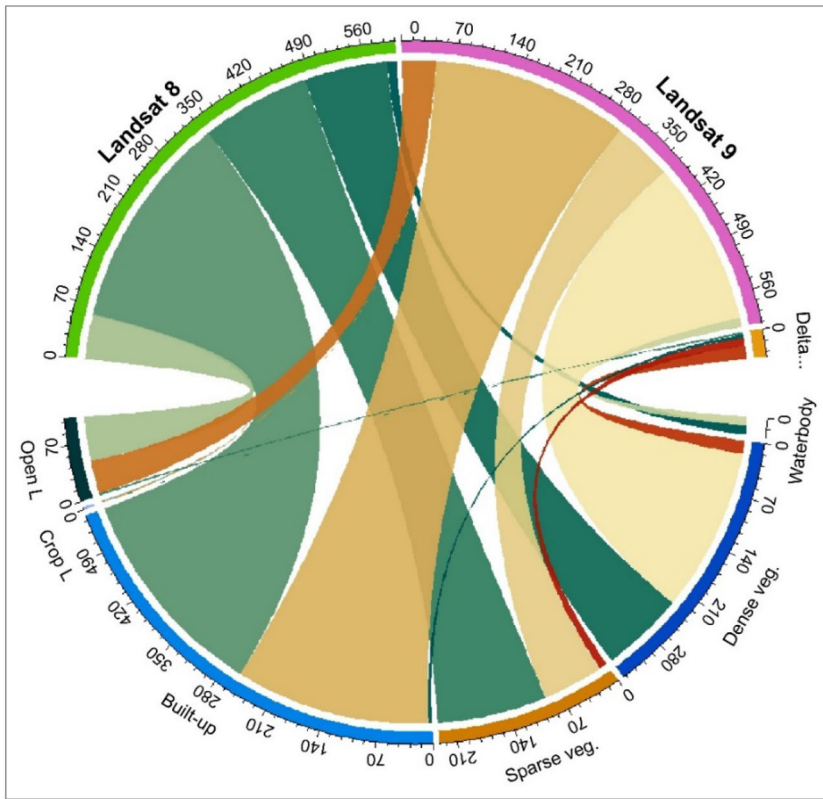


Figure 9. Quantification of land detection discrepancy between the LULC of Landsat 8 OLI and Landsat 9 OLI-2.

trustworthy LULC mapping and modeling, a minimum accuracy value of 80% is required. The total accuracy of the classification attained in this investigation meets the minimal accuracy criteria. The user and producer accuracies of the urban and water body classes, which are the classes of most significant interest in this research, are 84% and 93.2%, respectively, in OLI and 95% and 97.2% in OLI-2 (Table 2). Generally, water body detection using Landsat 8 is easy and has a high degree of accuracy, but the study area is predominated by built-up area and characterized by scanty water bodies. Therefore, using an OLI sensor, 84% accuracy is achieved, but it may be > 90% in other areas. A closer examination of the error matrix shows that distinguishing croplands from thick and sparse vegetation is difficult. The user and producer accuracies of urban areas for the LULC of OLI-2 in Table 3 are comparable to the LULC of OLI (97.2%), which are reasonably precise metrics. It is vital to remember that the accuracy of both the user and the producer is affected by various variables, including the number of random points created and the sampling technique used. The Kappa coefficient, which is a measure of agreement, may also determine categorization accuracy (Congalton 1991). The Kappa coefficient might seem to be low, giving the appearance that the value considers the actual agreement in the error matrix and the chance agreement (Congalton 1991). For the OLI and OLI-2 land cover maps, the Kappa coefficient was estimated to be 0.834 and 0.924, respectively. Therefore, based on the land discrepancy analysis and accuracy assessment, it can be stated that the LULC of the OLI-2 sensor outperformed the LULC of the OLI sensor, especially to detect dark objects like water bodies, dense vegetation, and sparse vegetation.

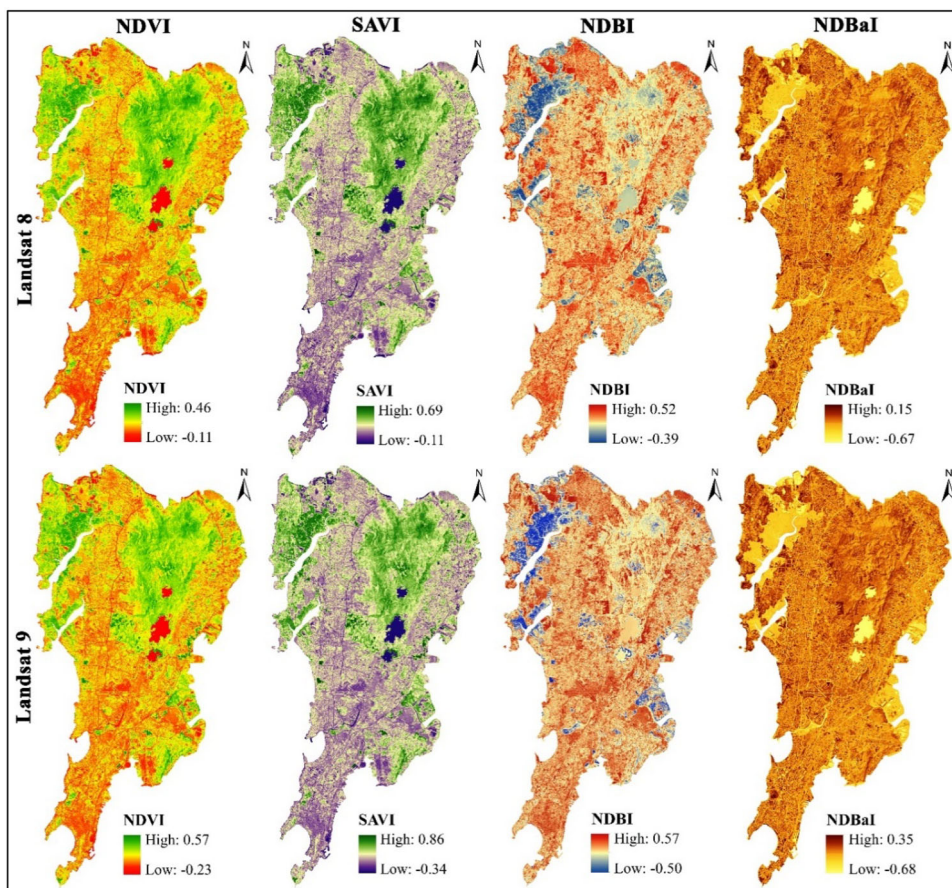


Figure 10. Surface biophysical parameters calculated from Landsat 8 OLI and Landsat 9 OLI-2 data sets.

3.5. Relationship between biophysical parameters and LULC of landsat 8 and 9

The bivariate local Moran's I (BiLISA cluster) has been used to detect the association between the LULC and surface biophysical parameters for Landsat 8 and 9 sensors. The results of the BiLISA cluster showed that the association between the LULC pattern and three surface biophysical parameters, i.e. NDMI, NDBaI, and NDWI, was not significant. Therefore, we removed these parameters from the final analysis. The NDMI is used to assess the soil moisture condition (Jin and Sader 2005), and it does not have a direct link with the LULC pattern. Hence, it does not have a significant association with the LULC pattern. The NDBaI is used to assess bare land (Chen et al. 2006), but in Mumbai city, the proportion of bare land is very low. Therefore, the association between NDBaI and LULC was also not significant. Moreover, the NDWI also does not show a very good association with LULC in comparison to the MNDWI. Therefore, it was also excluded from the final analysis.

The BiLISA map shows four different kinds of spatial correlations between LULC and surface biophysical parameters in Mumbai city (Figures 11 and 12). The result shows a striking agreement in the clustering pattern of LULC and NDVI spatial distributions of vegetation (dense and sparse vegetation combined) for Landsat 8. The high-high (HH) regions of NDVI are mainly predicted along the outskirts of the city (Figures 11b and f

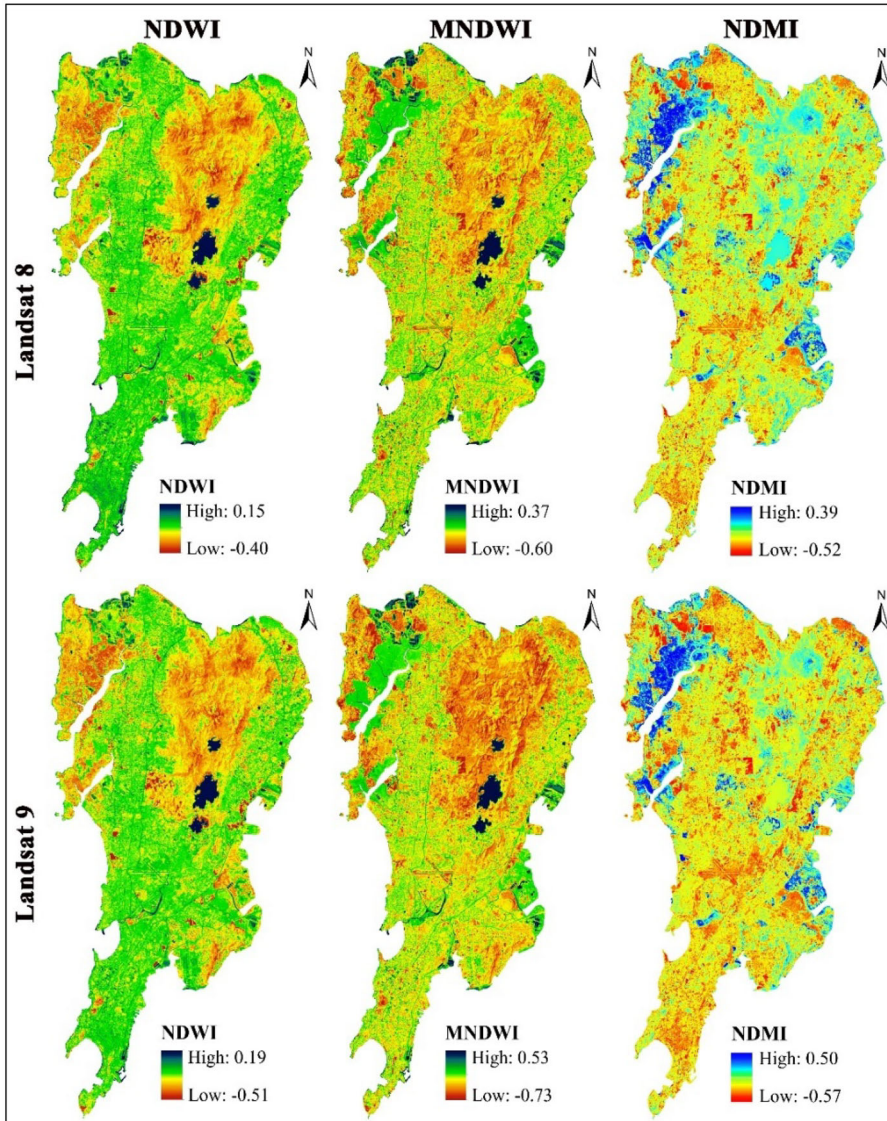


Figure 10. Continued

and 12b and f), while the area coverage is greater than SAVI (Figures 11c and g and 12c and g). The SAVI offers a clearer vegetation index image, while the NDVI catches certain water bodies. As a result, the geographical coverage of NDVI is greater since it takes into account aquatic bodies. The low-high (LH) regions were widely scattered across the city, with few exceptions. For Landsat 8, the high-low (HL) regions were spread throughout a reasonably small area for NDVI, MNDWI, and SAVI, while HH areas are concentrated in the core of the city in the case of built-up regions. The HL area is concentrated throughout Mumbai, whereas the LH area is concentrated on the outskirts of the city. In the case of Landsat 9, the MNDWI, NDVI, SAVI, and NDBI have all detected the highest concentration of HH near the water bodies, vegetation, and built-up areas. Furthermore, in the case of vegetation, HH regions cover more minor areas than Landsat 8 since it recognizes

Table 2. Validation of LULC map of landsat OLI.

LULC classes	Water body	Dense vegetation	Sparse vegetation	Built-up area	Cropland	Open land	Total	User's Accuracy	Kappa
Water body	32	4	2	0	0	0	38	0.84	–
Dense vegetation	0	29	4	0	2	0	35	0.828	–
Sparse vegetation	0	4	43	0	3	0	50	0.86	–
Built-up	0	0	0	109	0	8	117	0.932	–
Cropland	0	0	6	0	32	0	38	0.842	–
Open land	0	0	0	7	0	25	32	0.781	–
Total	32	37	55	116	37	33	310	0	–
Producer's Accuracy	1	0.784	0.782	0.939	0.864	0.581	0	0.87	–
Kappa	–	–	–	–	–	–	–	–	0.834

Table 3. Validation of LULC map of landsat OLI-2.

LULC classes	Water body	Dense vegetation	Sparse vegetation	Built-up area	Cropland	Open land	Total	User's Accuracy	Kappa
Water body	38	2	0	0	0	0	40	0.95	–
Dense vegetation	1	37	2	0	0	0	40	0.925	–
Sparse vegetation	0	0	41	0	2	0	43	0.953	–
Built-up	0	0	2	116	0	2	120	0.972	–
cropland	0	0	3	0	32	0	35	0.967	–
Open land	0	0	0	3	1	28	32	0.875	–
Total	39	39	48	119	35	30	310	0	–
Producer's Accuracy	0.974	0.948	0.854	0.975	0.914	0.933	0	0.941	–
Kappa	–	–	–	–	–	–	–	–	0.924

certain sections of bodies of water and built-up areas as vegetation. The same is true for built-up regions because Landsat 9 can find dark pixels better, so we can say that LULC and surface biophysical parameters can be accurately found.

4. Discussion

Although a number of satellite data sets have been used for the LULC mapping in different parts of the world, the Landsat data series is the most commonly used satellite data for the LULC mapping (Alam et al. 2020; Chaves et al. 2020). Landsat 9 OLI-2/TIRS-2, launched in September, 2021 from the Vandenberg Air Force Station in California, is the ninth satellite of the Landsat program, which is an upgraded version of the earlier Landsat satellite 8 OLI/TIRS, (Lulla et al. 2021). Although, both Landsat 8 OLI/TIRS and Landsat 9 OLI-2 have similar geometric and spatial characteristics, together they have increased the temporal resolution (revisit time) of the OLI sensor to 8 days. In this study, we have tried to compare the performance of the Landsat 8 OLI and Landsat 9 OLI-2 datasets in the LULC mapping. Although previously scholars have compared the performance of different satellite sensors (Forkuor et al. 2018; Ghayour et al. 2021) and techniques (Abdi 2020; Talukdar et al. 2020) in LULC mapping, no such study has been done

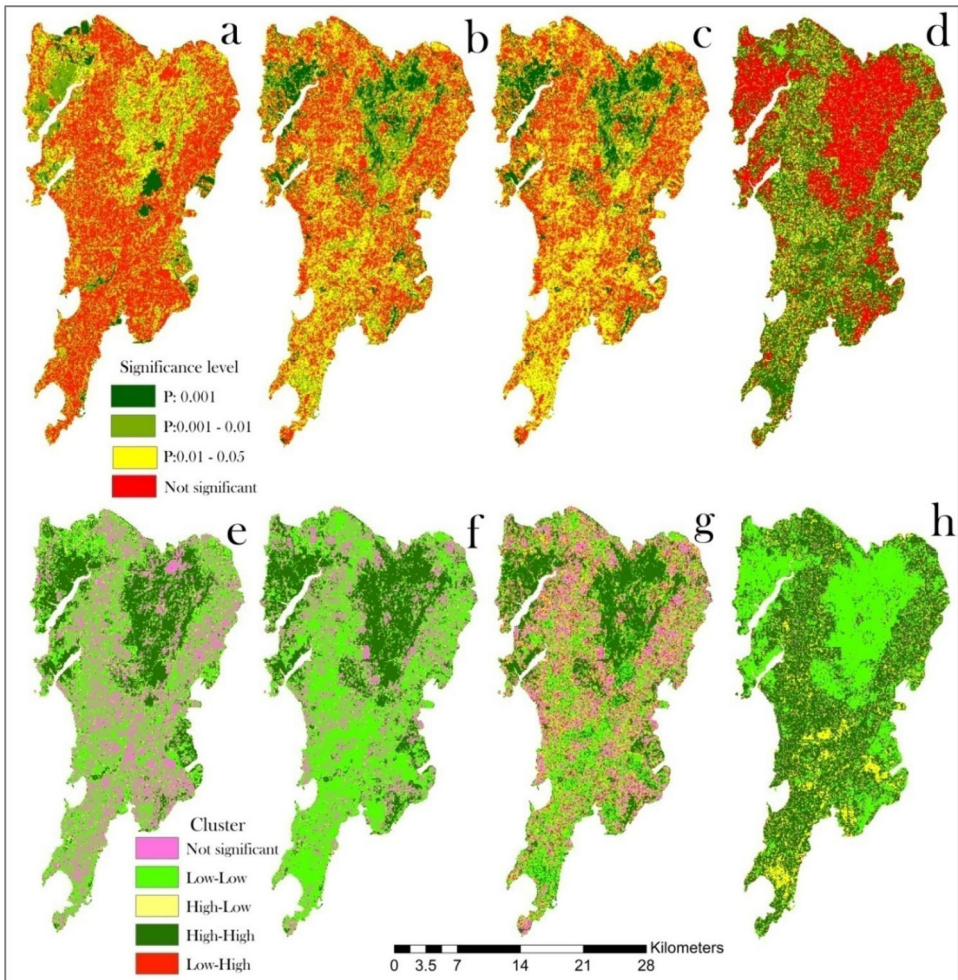


Figure 11. Significance analysis using bivariate local Moran's I for (a) LULC-MNDWI, (b) LULC-NDVI, (c) LULC-SAVI, and (d) LULC-NDBI, and cluster-dispersion analysis for (e) LULC-MNDWI, (f) LULC-NDVI, (g) LULC-SAVI, and (h) LULC-NDBI for Landsat 8.

for the OLI-2 data. Moreover, as per the authors' knowledge, this is the first study in which the LULC mapping has been done for the OLI-2 multispectral dataset.

The LULC classification from OLI and OLI-2 sensors has been done using the SVM machine learning algorithm. Further, the accuracy assessment has been done using the kappa coefficient. The study shows that the classification accuracy of both sensors is satisfactory (overall accuracy > 90%), but the OLI-2 data (overall accuracy > 98.00%) has outperformed the OLI data (overall accuracy > 91.7%). The accuracy of LULC classification from satellite datasets depends on a number of factors, like the resolution of the satellite data (Ullah et al. 2017), the approaches and techniques used (Talukdar et al. 2020; Balha et al. 2021), the training data (Shang et al. 2018), etc. In this study, the SVM has been applied for LULC classification using the same number of training samples. Further, the sensor characteristics of both OLI and OLI-2 are similar except for their radiometric calibration, which is higher for OLI-2 (14-bit) than OLI (12-bit). The accuracy over dark objects like dense vegetation cover was found to be higher for the OLI-2 (90.9%) than

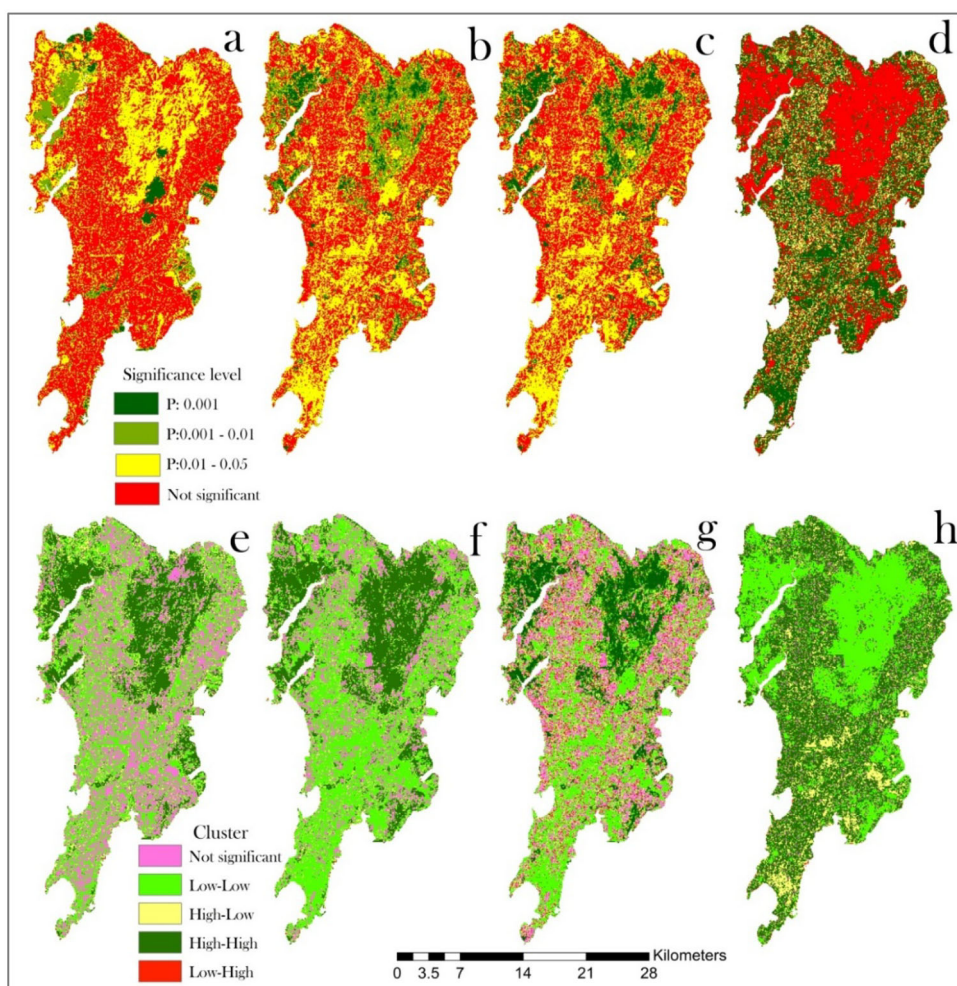


Figure 12. Significance analysis using bivariate local Moran's I for (a) LULC-MNDWI, (b) LULC-NDVI, (c) LULC-SAVI, and (d) LULC-NDBI, and cluster-dispersion analysis for (e) LULC-MNDWI, (f) LULC-NDVI, (g) LULC-SAVI, and (h) LULC-NDBI for Landsat 9.

that of the OLI data (86.6). At the same time, the accuracy of the built-up area was almost similar for both datasets. This illustrates that, the OLI-2 data is able to map the dark objects more precisely than the OLI data, which supports the assumption that OLI-2 has higher accuracy over darker objects due to its higher radiometric calibration (USGS 2021). However, the accuracy of a classified LULC map also depends on the spatial resolution of the satellite data, the quality of training samples, and the technique and software used for the LULC classification.

The surface biophysical parameters were also calculated from the multispectral bands of the OLI and OLI-2 datasets for the visual analysis and comparison of LULC classification with them. The surface biophysical parameters have been used as an indicator of LULC in a number of studies (Xue and Su 2017; Rasul et al. 2018; Shahfahad et al. 2020; Nandam and Patel 2021). In this study, we calculated seven biophysical parameters, but only four central bands of the OLI and OLI-2 datasets for the visual analysis and comparison of LULC classification with them. The surface biophysical parameters have been used

as an indicator of LULC in a number of studies (Xue and Su 2017; Rasul et al. 2018; Shahfahad et al. 2020; Nandam and Patel 2021). In this study, we calculated seven biophysical parameters, but only four (i.e. MNDWI, NDBI, NDVI, and SAVI) showed a significant relationship with the LULC pattern. Two parameters, i.e. NDBaI and NDMI, did not show any relationship with the LULC as the bare surface is very low in Mumbai and the moisture content is not retrieved in the LULC classification. The study showed that the MNDWI has better accuracy in showing water bodies than the NDWI in both OLI and OLI-2, hence, the NDWI was removed from the final analysis. Zhai et al. (2015) also noted a higher capability of the MNDWI for water detection from Landsat 5 TM and Landsat 7 ETM+ images. Among SAVI and NDVI, although SAVI was found to be more accurate in detecting the vegetation cover from both OLI and OLI-2 sensors. The object detection capability of NDVI was also high from both sensors. Moreover, the vegetation detection capability of SAVI has been noted to be higher for the OLI-2 sensor than OLI. The SAVI had shown a better vegetation detection capability than NDVI in several studies (Barati et al. 2011; Xue and Su 2017). The study also showed that the NDBI, SAVI, and MNDWI were found to be the best indices for the mapping of built-up area, vegetation cover, and water bodies, respectively, as they showed a significant relationship with the LULC classification in both Moran's I and cluster-dispersion analysis.

The study further showed that although both OLI and OLI-2 sensors have produced reliable results in the LULC mapping with satisfactory accuracy, the accuracy of the OLI-2 sensor is comparatively higher. Therefore, it may be stated that the Landsat 9 OLI-2 data have increased the performance of the Landsat data series in monitoring the earth's surface features. Hence, the application of OLI-2 images in LULC mapping may increase its accuracy, which may be better for preparing land use plans at various levels. For future studies, it is suggested to make a comparison of different LULC classifiers for LULC mapping using the OLI-2 dataset. Previously, Talukdar et al. (2020) did the same for OLI data and noted that SVM and RF were the best classifiers for LULC mapping using OLI data. Hence, a comparison of different classifiers for LULC mapping from OLI-2 data may help in finding the best classifier for LULC mapping from OLI-2 data.

5. Conclusion

In the present study, an evaluation of the performance of the Landsat 8 OLI and Landsat 9 OLI-2 multispectral datasets has been done for the LULC mapping over a heterogeneous urban surface. For the LULC classification, the SVM technique has been applied using QGIS software. Seven surface biophysical parameters (NDVI, SAVI, NDBI, NDBaI, NDWI, MNDWI, & NDMI) were extracted from the multispectral bands of both satellites for a comparative analysis. The study shows that the LULC classification from both OLI and OLI-2 sensors exhibited similar LULC patterns and has produced reliable accuracy in LULC mapping (overall accuracy of 83.4% and 92.4%, respectively). The accuracy of the OLI-2 LULC map is comparatively higher. The comparison of classified LULC maps from Google Earth imagery also shows some portions of vegetation cover and built-up areas have been classified as open land in the LULC map of the OLI image while they have been correctly classified in the LULC map of OLI-2. Moreover, the LULC classification from OLI-2 also showed some errors, as some portions of open land have been classified as the built-up area in the LULC map of OLI-2. The land detection discrepancy using the Markovian transition matrix describes that although the OLI and OLI-2 sensors have some difference in their capability of object detection, both of them have detected the LULC features with about 80% accuracy. The change detection between the LULC of the

OLI and OLI-2 sensors also showed some variation in the area under each LULC class. The comparison of surface biophysical parameters (spectral indices) using bivariate local Moran's I and BiLISA clusters shows that only four biophysical parameters (NDVI, SAVI, NDBI, and MNDWI) have a significant relationship with the LULC maps in both OLI and OLI-2. Furthermore, in the case of OLI-2, the relationships of SAVI and MNDWI with LULC maps were found to be stronger, whereas NDVI and NDBI showed a similar relationship with LULC maps in both sensors. Based on this analysis, it can be concluded that the Landsat 9 (OLI-2) data is better for precise mapping of the earth's surface features.

Authors contribution

Shahfahad, Swapan Talukdar and Mohd Waseem Naikoo: conceptualization, data curation, data analysis and writing original draft. Atiqur Rahman and A.S. Gagnon: mapping, review & editing and supervision. Abu Reza Md Towfiqul Islam and Amir Mosavi: Data collection, data analysis and designing.

Disclosure statement

No potential conflict of interest was reported by the authors.

ORCID

Shahfahad  <http://orcid.org/0000-0001-5868-1062>
 Swapan Talukdar  <http://orcid.org/0000-0001-6680-9791>
 Mohd Waseem Naikoo  <http://orcid.org/0000-0001-5779-9325>
 Atiqur Rahman  <http://orcid.org/0000-0002-9001-5059>
 Alexandre S. Gagnon  <http://orcid.org/0000-0002-1301-6015>
 Abu Reza Md Towfiqul Islam  <http://orcid.org/0000-0001-5779-1382>

Data availability statement

The data will be available upon reasonable request through corresponding authors.

References

- Abdi AM. 2020. Land cover and land use classification performance of machine learning algorithms in a boreal landscape using Sentinel-2 data. *GISci Remote Sens.* 57(1):1–20.
- Adam E, Mutanga O, Odindi J, Abdel-Rahman EM. 2014. Land-use/cover classification in a heterogeneous coastal landscape using RapidEye imagery: evaluating the performance of random forest and support vector machines classifiers. *Int J Remote Sens.* 35(10):3440–3458.
- Adnan MSG, Abdullah AYM, Dewan A, Hall JW. 2020. The effects of changing land use and flood hazard on poverty in coastal Bangladesh. *Land Use Policy.* 99:104868.
- Alam A, Bhat MS, Maheen M. 2020. Using Landsat satellite data for assessing the land use and land cover change in Kashmir valley. *GeoJournal.* 85(6):1529–1543.
- Amolins K, Zhang Y, Dare P. 2007. Wavelet based image fusion techniques—An introduction, review and comparison. *ISPRS J Photogramm Remote Sens.* 62(4):249–263.
- Anderson JR. 1976. A land use and land cover classification system for use with remote sensor data. Vol. 964. Geological Survey Professional Paper 964. Washington (DC): US Government Printing Office.
- Anselin L, Syabri I, Smirnov O. 2002. Visualizing multivariate spatial correlation with dynamically linked windows. “Visualizing Multivariate Spatial Correlation with Dynamically Linked Windows.” In “New Tools in Spatial Data Analysis.” Proceedings of a Workshop. Center for Spatially Integrated Social Science, University of California, edited by L. Anselin and S. Rey, Santa Barbara: CDROM.

- Arvidson T, Goward S, Gasch J, Williams D. 2006. Landsat-7 long-term acquisition plan. *Photogramm Eng Remote Sensing*. 72(10):1137–1146.
- Azeez A, Gnanappazham L, Muraleedharan KR, Revichandran C, John S, Seena G, Thomas J. 2022. Multi-decadal changes of mangrove forest and its response to the tidal dynamics of thane creek, Mumbai. *J Sea Res*. 180:102162.
- Balha A, Mallick J, Pandey S, Gupta S, Singh CK. 2021. A comparative analysis of different pixel and object-based classification algorithms using multi-source high spatial resolution satellite data for LULC mapping. *Earth Sci Inform*. 14(4):2231–2247.
- Barati S, Rayegani B, Saati M, Sharifi A, Nasri M. 2011. Comparison the accuracies of different spectral indices for estimation of vegetation cover fraction in sparse vegetated areas. *Egyptian J Remote Sens Space Sci*. 14(1):49–56.
- Bauer ME. 2020. Remote sensing of environment: history, philosophy, approach and contributions, 1969–2019. *Remote Sens Environ*. 237:111522.
- Census of India. 2011. Mumbai (Greater Mumbai) Metropolitan Population 2011 – 2022. Census. <https://www.census2011.co.in/census/metropolitan/305-mumbai.html>.
- Chachondhia P, Shakya A, Kumar G. 2021. Performance evaluation of machine learning algorithms using optical and microwave data for LULC classification. *Remote Sens Appl: Soc Environ*. 23:100599.
- Chander G, Coan MJ, Scaramuzza PL. 2008. Evaluation and comparison of the IRS-P6 and the Landsat sensors. *IEEE Trans Geosci Remote Sensing*. 46(1):209–221.
- Chaves MED, Picoli MCA, Sanches ID. 2020. Recent applications of Landsat 8/OLI and Sentinel-2/MSI for land use and land cover mapping: a systematic review. *Remote Sens*. 12(18):3062.
- Chen W, Li X, He H, Wang L. 2017. A review of fine-scale land use and land cover classification in open-pit mining areas by remote sensing techniques. *Remote Sens*. 10(2):15.
- Chen XL, Zhao HM, Li PX, Yin ZY. 2006. Remote sensing image-based analysis of the relationship between urban heat island and land use/cover changes. *Remote Sens Environ*. 104(2):133–146.
- Choate MJ, Rengarajan R, Storey JC, Lubke M. 2022. Landsat 9 geometric characteristics using underfly data. *Remote Sens*. 14(15):3781.
- Congalton RG. 1991. A review of assessing the accuracy of classifications of remotely sensed data. *Remote Sens Environ*. 37(1):35–46.
- Congalton RG. 2010. Remote sensing: an overview. *GIScience & Remote Sens*. 47(4):443–459.
- Das N, Mondal P, Sutradhar S, Ghosh R. 2021. Assessment of variation of land use/land cover and its impact on land surface temperature of Asansol subdivision. *Egyptian J Remote Sens Space Sci*. 24(1):131–149.
- Dwyer JL, Roy DP, Sauer B, Jenkerson CB, Zhang HK, Lymburner L. 2018. Analysis ready data: enabling analysis of the Landsat archive. *Remote Sens*. 10(9):1363.
- Egorov AV, Roy DP, Zhang HK, Li Z, Yan L, Huang H. 2019. Landsat 4, 5 and 7 (1982 to 2017) Analysis Ready Data (ARD) observation coverage over the conterminous United States and implications for terrestrial monitoring. *Remote Sens*. 11(4):447.
- Ellis EC, Gauthier N, Goldewijk KK, Bird RB, Boivin N, Díaz S, Fuller DQ, Gill JL, Kaplan JO, Kingston N, et al. 2021. People have shaped most of terrestrial nature for at least 12,000 years. *Proc Natl Acad Sci USA*. 118(17):e2023483118.
- Forkuor G, Dimobe K, Serme I, Tondoh JE. 2018. Landsat-8 vs. Sentinel-2: examining the added value of sentinel-2's red-edge bands to land-use and land-cover mapping in Burkina Faso. *GIScience & Remote Sens*. 55(3):331–354.
- Fu W, Ma J, Chen P, Chen F. 2020. Remote sensing satellites for digital earth. In: *Manual of digital earth*. Singapore: Springer; p. 55–123.
- Ghayour L, Neshat A, Paryani S, Shahabi H, Shirzadi A, Chen W, Al-Ansari N, Geertsema M, Amiri MP, Gholamnia M, et al. 2021. Performance evaluation of sentinel-2 and landsat 8 OLI data for land cover/use classification using a comparison between machine learning algorithms. *Remote Sens*. 13(7):1349.
- Goward SN, Masek JG, Williams DL, Irons JR, Thompson RJ. 2001. The Landsat 7 mission: terrestrial research and applications for the 21st century. *Remote Sens Environ*. 78(1-2):3–12.
- Hemati M, Hasanlou M, Mahdianpari M, Mohammadimanesh F. 2021. A systematic review of landsat data for change detection applications: 50 years of monitoring the earth. *Remote Sens*. 13(15):2869.
- Huete AR. 1988. A soil-adjusted vegetation index (SAVI). *Remote Sens Environ*. 25(3):295–309.
- Hütt C, Koppe W, Miao Y, Bareth G. 2016. Best Accuracy Land Use/land Cover (LULC) Classification to Derive Crop Types Using Multitemporal, Multisensor, and Multi-Polarization SAR Satellite Images. *Remote Sensing*. 8(8):684.doi:10.3390/rs8080684.
- Jin S, Sader SA. 2005. Comparison of time series tasseled cap wetness and the normalized difference moisture index in detecting forest disturbances. *Remote Sens Environ*. 94(3):364–372.

- Kamaraj NP, Shekhar S, Sivashankari V, Balasubramani K, Prasad KA. 2021. Detecting heat-inducing urban built-up surface material with multi remote sensing datasets using reflectance and emission spectroscopy. *Remote Sens Environ.* 264:112591.
- Kaur H, Koundal D, Kadyan V. 2021. Image fusion techniques: a survey. *Arch Comput Methods Eng.* 28(7):4425–4447.
- Kotthaus S, Smith TE, Wooster MJ, Grimmond CSB. 2014. Derivation of an urban materials spectral library through emittance and reflectance spectroscopy. *ISPRS J Photogramm Remote Sens.* 94: 194–212.
- Kriegler FJ, Malila WA, Nalepka RF, Richardson W. 1969. Preprocessing transformations and their effects on multi-spectral recognition. In *Proceedings of the Sixth International Symposium on Remote Sensing of Environment*. Ann Arbor, MI: University of Michigan; p. 97–131.
- Lambin EF, Meyfroidt P. 2011. Global land use change, economic globalization, and the looming land scarcity. *Proc Natl Acad Sci U S A.* 108(9):3465–3472.
- Lulla K, Nellis MD, Rundquist B, Srivastava PK, Szabo S. 2021. Mission to earth: LANDSAT 9 will continue to view the world. *Geocarto Int.* 36(20):2261–2263.
- Mahyari AG, Yazdi M. 2011. Panchromatic and multispectral image fusion based on maximization of both spectral and spatial similarities. *IEEE Trans Geosci Remote Sensing.* 49(6):1976–1985.
- Malleswara Rao J, Siddiqui A, Maithani S, Kumar P. 2020. Hyperspectral and multispectral data fusion using fast discrete curvelet transform for urban surface material characterization. *Geocarto Int.* 37(7): 2018–2030.
- Mallick J, Talukdar S, Pal S, Rahman A, Shahfahad . 2021. A novel classifier for improving wetland mapping by integrating image fusion techniques and ensemble machine learning classifiers. *Ecol Inf.* 65: 101426.
- Masek JG, Wulder MA, Markham B, McCorkel J, Crawford CJ, Storey J, Jenstrom DT. 2020. Landsat 9: empowering open science and applications through continuity. *Remote Sens Environ.* 248:111968.
- McFeeters SK. 1996. The use of the Normalized Difference Water Index (NDWI) in the delineation of open water features. *Int J Remote Sens.* 17(7):1425–1432.
- Mhangara P, Mapurisa W, Mudau N. 2020. Comparison of image fusion techniques using satellite pour l'Observation de la Terre (SPOT) 6 satellite imagery. *Appl Sci.* 10(5):1881.
- Naikoo MW, Rihan M, Peer AH, Talukdar S, Mallick J, Ishtiaq M, Rahman A. 2022. Analysis of peri-urban land use/land cover change and its drivers using geospatial techniques and geographically weighted regression. *Environ Sci Pollut Res*:1–19. doi:10.1007/s11356-022-18853-4
- Nandam V, Patel PL. 2021. A novel hybrid approach using SVM and spectral indices for enhanced land use land cover mapping of coastal urban plains. *Geocarto Int.* 37(16):4714–4736.
- Noble WS. 2006. What is a support vector machine? *Nat Biotechnol.* 24(12):1565–1567.
- NRSC. 1995. Natural resource census- land use land cover database. Technical Report–Ver.1. [accessed 2022 April]. <https://bhuvan-app1.nrsc.gov.in/2dresources/thematic/2LULC/lulc1112.pdf>.
- Oldoni LV, Mercante E, Antunes JFG, Cattani CEV, Silva Junior CAD, Caon IL, Prudente VHR. 2021. Extraction of crop information through the spatiotemporal fusion of OLI and MODIS images. *Geocarto Int*:1–25. doi:10.1080/10106049.2021.2000648
- Overmars KD, De Koning GHJ, Veldkamp A. 2003. Spatial autocorrelation in multi-scale land use models. *Ecol Modell.* 164(2–3):257–270.
- Pethe A, Nallathiga R, Gandhi S, Tandel V. 2014. Re-thinking urban planning in India: Learning from the wedge between the de jure and de facto development in Mumbai. *Cities.* 39:120–132.
- Phan DC, Trung TH, Truong VT, Sasagawa T, Vu TPT, Bui DT, Hayashi M, Tadono T, Nasahara KN. 2021. First comprehensive quantification of annual land use/cover from 1990 to 2020 across mainland Vietnam. *Sci Rep.* 11(1):1–20.
- Phiri D, Morgenroth J, Xu C, Hermosilla T. 2018. Effects of pre-processing methods on Landsat OLI-8 land cover classification using OBIA and random forests classifier. *Int J Appl Earth Obs Geoinf.* 73: 170–178.
- Praveen B, Talukdar S, Mahato S, Mondal J, Sharma P, Islam ARMT, Rahman, A, Shahfahad . 2020. Analyzing trend and forecasting of rainfall changes in India using non-parametrical and machine learning approaches. *Sci Rep.* 10(1):1–21.
- Rahman A, Aggarwal SP, Netzband M, Fazal S. 2011. Monitoring urban sprawl using remote sensing and GIS techniques of a fast growing urban centre, India. *IEEE J Sel Top Appl Earth Observations Remote Sens.* 4(1):56–64.
- Rasul A, Balzter H, Ibrahim GRF, Hameed HM, Wheeler J, Adamu B, Ibrahim S, Najmaddin PM. 2018. Applying built-up and bare-soil indices from Landsat 8 to cities in dry climates. *Land.* 7(3):81.

- Rihan M, Naikoo MW, Ali MA, Usmani TM, Rahman A. **2021**. Urban heat island dynamics in response to land-use/land-cover change in the coastal city of Mumbai. *J Indian Soc Remote Sens.* 49(9): 2227–2247.
- Ritchie JC, Zimba PV, Everitt JH. **2003**. Remote sensing techniques to assess water quality. *Photogramm Eng Remote Sens.* 69(6):695–704.
- Roy DP, Wulder MA, Loveland TR, Woodcock CE, Allen RG, Anderson MC, Helder D, Irons JR, Johnson DM, Kennedy R, Scambos TA, et al. **2014**. Landsat-8: science and product vision for terrestrial global change research. *Remote Sens Environ.* 145:154–172.
- Shahfahad , Kumari B, Tayyab M, Ahmed IA, Baig MRI, Khan MF, Rahman A. **2020**. Longitudinal study of land surface temperature (LST) using mono-and split-window algorithms and its relationship with NDVI and NDBI over selected metro cities of India. *Arab J Geosci.* 13(19):1–19.
- Shahfahad , Naikoo MW, Towfiqul Islam ARM, Mallick J, Rahman A. **2022**. Land use/land cover change and its impact on surface urban heat island and urban thermal comfort in a metropolitan city. *Urban Climate.* 41:101052.
- Shang M, Wang SX, Zhou Y, Du C. **2018**. Effects of training samples and classifiers on classification of landsat-8 imagery. *J Indian Soc Remote Sens.* 46(9):1333–1340.
- Shih HC, Stow DA, Chang KC, Roberts DA, Goulias KG. **2021**. From land cover to land use: applying random forest classifier to Landsat imagery for urban land-use change mapping. *Geocarto Int.* 37(19): 5523–5546.
- Singh RK, Singh P, Drews M, Kumar P, Singh H, Gupta AK, Govil H, Kaur A, Kumar M. **2021**. A machine learning-based classification of LANDSAT images to map land use and land cover of India. *Remote Sens Appl: soc Environ.* 24:100624.
- Song C, Woodcock CE, Seto KC, Lenney MP, Macomber SA. **2001**. Classification and change detection using Landsat TM data: when and how to correct atmospheric effects? *Remote Sens Environ.* 75(2): 230–244.
- Stephens L, Fuller D, Boivin N, Rick T, Gauthier N, Kay A, Marwick B, Armstrong CG, Barton CM, Denham T, et al. **2019**. Archaeological assessment reveals Earth’s early transformation through land use. *Science.* 365(6456):897–902.,
- Talukdar S, Mankotia S, Shamimuzzaman M, Mahato S. **2021b**. Wetland-inundated area modeling and monitoring using supervised and machine learning classifiers. In: Pandey PC, Sharma LK, editors. *Advances in remote sensing for natural resource monitoring*. United States: Wiley-Blackwell; p. 346–365.
- Talukdar S, Salam R, Samad A, Rihan M, Rahman A. **2021a**. Improving wetland mapping techniques using the integration of image fusion techniques and artificial neural network (ANN). In: Shit PK, Das P, Bhunia GS, Dutta D, editors. *Mapping, monitoring, and modeling land and water resources*. United States: CRC Press; p. 149–164.
- Talukdar S, Singha P, Mahato S, Pal S, Liou Y-A, Rahman, A, Shahfahad . **2020**. Land-use land-cover classification by machine learning classifiers for satellite observations—A review. *Remote Sens.* 12(7): 1135.
- Ullah S, Shafique M, Farooq M, Zeeshan M, Dees M. **2017**. Evaluating the impact of classification algorithms and spatial resolution on the accuracy of land cover mapping in a mountain environment in Pakistan. *Arab J Geosci.* 10(3):1–11.
- USGS. **2021**. Landsat 9 data users handbook. Department of the Interior U.S. Geological Survey. <https://www.usgs.gov/media/files/landsat-9-data-users-handbook>.
- Wentz EA, Anderson S, Fragkias M, Netzband M, Mesev V, Myint SW, Quattrochi D, Rahman A, Seto KC. **2014**. Supporting global environmental change research: a review of trends and knowledge gaps in urban remote sensing. *Remote Sensing.* 6(5):3879–3905.
- Winkler K, Fuchs R, Rounsevell M, Herold M. **2021**. Global land use changes are four times greater than previously estimated. *Nat Commun.* 12(1):1–10.
- Wulder MA, Loveland TR, Roy DP, Crawford CJ, Masek JG, Woodcock CE, Allen RG, Anderson MC, Belward AS, Cohen WB, et al. **2019**. Current status of Landsat program, science, and applications. *Remote Sens Environ.* 225:127–147.
- Wulder MA, White JC, Loveland TR, Woodcock CE, Belward AS, Cohen WB, Fosnight EA, Shaw J, Masek JG, Roy DP. **2016**. The global Landsat archive: status, consolidation, and direction. *Remote Sens Environ.* 185:271–283.
- Xu H. **2006**. Modification of normalised difference water index (NDWI) to enhance open water features in remotely sensed imagery. *Int J Remote Sens.* 27(14):3025–3033.
- Xue J, Su B. **2017**. Significant remote sensing vegetation indices: a review of developments and applications. *J Sensors*, 2017:1353691. doi:10.1155/2017/1353691

- Yılmaz A, Küçükler A, Bayrak G, Ertekin D, Shafie-Khah M, Guerrero JM. 2022. An improved automated PQD classification method for distributed generators with hybrid SVM-based approach using un-decimated wavelet transform. *Int J Electr Power & Energy Syst.* 136:107763.
- Young NE, Anderson RS, Chignell SM, Vorster AG, Lawrence R, Evangelista PH. 2017. A survival guide to Landsat preprocessing. *Ecology.* 98(4):920–932.
- Yunhao C, Lei D, Jing L, Xiaobing L, Peijun S. 2006. A new wavelet-based image fusion method for remotely sensed data. *Int J Remote Sens.* 27(7):1465–1476.
- Zha Y, Gao J, Ni S. 2003. Use of normalized difference built-up index in automatically mapping urban areas from TM imagery. *Int J Remote Sens.* 24(3):583–594.
- Zhai K, Wu X, Qin Y, Du P. 2015. Comparison of surface water extraction performances of different classic water indices using OLI and TM imageries in different situations. *Geo-Spatial Inform Sci.* 18(1): 32–42.
- Zhou G, Chen W, Gui Q, Li X, Wang L. 2021. Split depth-wise separable graph-convolution network for road extraction in complex environments from high-resolution remote-sensing Images. *IEEE Trans Geosci Remote Sens.* 60:1–15.